Investigation of Microbubble Boundary Layer Using Particle Tracking Velocimetry

Javier Ortiz-Villafuerte[1]

Yassin A Hassan[2]
e-mail: y-hassan@tamu.edu

Department of Nuclear Engineering,
Texas A&M University,
College Station, TX 77843-3133

Particle tracking velocimetry has been used to measure the velocity fields of both continuous phase and dispersed microbubble phase, in a turbulent boundary layer, of a channel flow. Hydrogen and oxygen microbubbles were generated by electrolysis. The average size of the microbubbles was 15 μm in radius. Drag reductions up to 40% were obtained, when the accumulation of microbubbles took place in a critical zone within the buffer layer. It is confirmed that a combination of concentration and distribution of microbubbles in the boundary layer can achieve high drag reduction values. Microbubble distribution across the boundary layer and their influence on the profile of the components of the liquid mean velocity vector are presented. The spanwise component of the mean vorticity field was inferred from the measured velocity fields. A decrease in the magnitude of the vorticity is found, leading to an increase of the viscous sublayer thickness. This behavior is similar to the observation of drag reduction by polymer and surfactant injection into liquid flows. The results obtained indicate that drag reduction by microbubble injection is not a simple consequence of density effects, but is an active and dynamic interaction between the turbulence structure in the buffer zone and the distribution of the microbubbles. [DOI: 10.1115/1.2174062]

Keywords: drag reduction, microbubbles, PIV, PTV

1 Introduction

A renewed interest for drag reduction technologies and research has been noticed during the last few years. Much research has been performed with polymer and surfactants injection in duct and boundary layer flows. Alternatively, drag reduction due to microbubble injection in turbulent boundary layers has also gained attention, because of its environmental friendship. This type of drag reduction is particularly important for maritime transportation applications, since 80% of the total drag in a large ship is due to skin friction [1]. Minimizing the drag encountered by vehicles moving in air or water and the fluid resistance in gas, water, or oil pipelines leads to saving in fuel consumption. When higher rates of mass, momentum, or heat transfer are desired, it is imperative that the concomitant drag penalty be kept to a minimum. Reducing drag saves enormous resources spent to overcome it and is clearly advantageous to the environment, the economy, and the overall industrial competitiveness [2].

McCormick and Bhattacharyya [3] showed a significant reduction of frictional resistance can be achieved using microbubbles, at low void fractions. In their work, hydrogen microbubbles generated by electrolysis produced up to 30% drag reduction over a body of revolution with less than 1% void fraction. They also showed that as the Reynolds number of the liquid increased, the effectiveness of microbubbles in reducing drag diminished with the same gas injection rate. This is also obtained at high Reynolds numbers of 10^8 that was reported in a recent experiment over a flat plate [4]. Moreover, the drag reduction degree of persistence was greater at lower speeds with a given gas injection rate, and the drag reduction increased with the increase of gas injection rate.

As in polymer drag reduction, microbubbles have been shown the capability of achieving drag reductions as high as 80% on flat plate boundary layers [5]. By combining polymers and microbubbles, Fontaine et al. [6] achieved drag reductions greater than 80%. They suggested that polymer drag reduction was independent of the mechanism responsible for the microbubble skin friction reduction. Takahashi et al. [7] reported skin friction reduction up to 32% on a 50 m long ship model.

Despite many studies on microbubble drag reduction, there is no complete agreement on the microbubble physical phenomena leading to drag reduction. Issues such as microbubble size and distribution in the boundary layer have been recognized as key parameters in achieving important gains in drag reduction, but the role of such parameters is not yet fully understood. Microbubble generation is another important issue, since the net energy saving in a system must account for the energy required to produce the microbubbles. Generally, large amounts of gas are required to reach high levels of drag reduction. Experimental studies have shown, however, that microbubbles with size of the same order of the length scale of the liquid phase turbulence perform better in achieving drag reduction, and lower gas injection rates are required [8].

Among the main factors considered responsible for the microbubble drag reduction phenomena are the decrease of density, the increase of effective viscosity, and the liquid turbulence-microbubble interactions. Buoyancy effects in microbubble drag reduction have been reported by Madavant et al. [5] and Sanders et al. [4]. In a flat plate boundary layer, Madavan et al. achieved higher drag reduction in their plate-on-top experiment than in the plate-on-bottom case. Sanders et al. reached almost 100% drag reduction when the injected gas formed a layer underneath the flat plate. The increase of the void fraction increases the local effective viscosity and reduces the turbulent momentum transfer [9,10]. Turbulence modification of the liquid boundary layer has been measured by Kitagawa et al. [11]. They measured an increase of both nondimensional streamwise and normal turbulence intensities, and a decrease of the Reynolds stress, with void fraction increase.

Numerical simulations have been used also as a means to in-

[1]Currently at Department of Nuclear Systems, National Institute for Nuclear Research, Ocoyoacac, Mexico 52045.

[2]Corresponding author.

Contributed by the Fluids Engineering Division of ASME for publication in the Journal of Fluids Engineering. Manuscript received March 31, 2004; final manuscript received October 11, 2005. Review conducted by Joseph Katz.

vestigate the underlying mechanism of microbubble drag reduction. Madavan et al. [12] determined that microbubble size and distribution in the boundary layer were major issues in the microbubble drag reduction phenomena. Similar results were found by Xu et al. [13] with a direct numerical simulation (DNS) of a fully developed turbulent channel flow using a force-coupling method (FCM). Their results indicate that the initial seeding of microbubbles has an important effect on the pressure gradient and viscous drag force. Furthermore, smaller microbubbles gave a sustained reduction in drag, while larger bubbles only exhibited transient drag reduction. A reduction in mean drag of 6.2% was achieved at a void fraction of 4.24%. The microbubbles were seeded from a location having a distance from the wall of $y^+ = 20$. Recently, Ferrante and Elghobashi [14] performed a DNS on a spatially developing turbulent boundary layer over a flat plate with microbubbles injection. They obtained a maximum drag reduction of 20.2% at a void fraction of 2%. They concluded that the drag reduction was caused by a velocity divergence effect, associated with the void fraction. The presence of microbubbles generates a local positive divergence of the fluid velocity, creating a positive mean normal velocity at a farther distance from the wall. This reduces the mean streamwise velocity and displaces the quasistreamwise longitudinal vortical structures away from the wall due to the presence of bubbles. This displacement increases the spanwise gaps between the wall streaks associated with the sweep events and reduces the streamwise velocity of these streaks.

Although DNS of microbubble turbulent boundary layers provides insight into the physical phenomena responsible for the drag reduction, it is not currently feasible to use it for practical designs of maritime and other transportation means that could take advantage of the drag reduction phenomenon. Thus, multiphase Reynolds averaged Navier-Stokes (RANS) methods are being developed for simulations of three-dimensional geometries at relevant high Reynolds numbers [15,16].

In this paper, particle tracking velocimetry (PTV) is used to obtain velocity components of both continuous and microbubble dispersed particle image velocimetry (PIV) images. It is shown that microbubbles with an average radius of 15 μm flowing in the buffer layer can produce drag reductions of about 40%. This confirms the necessity of a specific concentration of microbubbles in the buffer zone of the boundary layer to achieve high drag reductions. The modification of the components of the liquid mean velocity distributions across the boundary layer is presented for different drag reductions. Further, the vorticity modification due to the presence of microbubbles in a channel turbulent boundary layer was investigated. Vorticity fields of the two phase flow at different drag reductions are presented and compared.

Experimental Setup

A flow facility was constructed to study the turbulent boundary layer in a channel flow. A schematic of the flow system used in this experiment is illustrated in Fig. 1. One of the supply tanks is located 2.85 m above the channel level. In normal operation, the pumped water into the upper tank exceeds the flow that can be delivered to the channel through a 2.54 cm diameter hose; thus, it ensures a constant pressure head. When it is full, it provides a constant water column of 3.65 m. Its capacity is 0.21 m^3. This tank is also used as a phase separator, to avoid air flowing into the channel, and to assure a single-phase water flow. The other tank is about 1 m below the channel level. Its capacity is 0.35 m^3. This tank receives the overflow from the upper tank, and it is also used to mix the seed tracer particles with the flow. The chanel is made of 12.7 mm thick Plexiglas. Its length is 3.05 m, and the cross-sectional area A is 15 cm $\times$ 8.81 cm. The center of the measurement area was located at 205.62 cm from the inlet nozzle and 45.88 cm from the exit nozzle. The inlet nozzle has plastic screens and flow straighteners to ensure a uniform flow. Two water filters with several filter layers prevented any particles larger than 10 μm to flow into the channel. Prior to each test, the water is continuously run through the filter, to ensure that only the seed tracers will be flowing during the measurements. The flow was seeded with 6 μm polystyrene tracer particles. Their density is 1050 kg/m^3. A volumetric flow rate Q of 1.02×10^{-3} m^3/s was used, and the obtained averaged cross-sectional velocity $u_m = Q/A$ was 7.72×10^{-2} m/s.

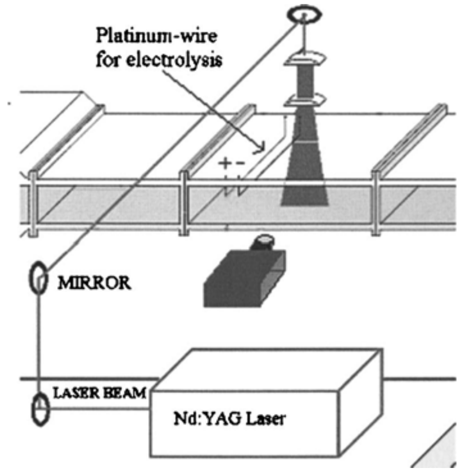

Fig. 1 Sketch of the PIV setup

Two platinum (Pt) wires each with a diameter of 76 μm was located about 1 cm from the channel upper wall. These wires serve as cathode and anode for microbubble generation via electrolysis. The first wire was located at a distance of 35.56 cm, while the second wire, the anode, was at 11.43 cm along the streamwise direction from the measurement area. When the power supply delivers its current, hydrogen bubbles are produced on the anode, while oxygen bubbles are generated on the cathode. The anode produces a higher bubble density than the cathode, and the bubbles are smaller. The influence of the Pt wires on the flow is negligible, since the Reynolds number based on the wire diameter is less than 10, and the wire is located at more than 1500 wire diameters from the measurement zone.

The PIV system consisted of a high power laser, a high resolution charge coupled device (CCD) camera, a pulse generator, and acquisition boards and software. The illumination source for the PIV system was a dual oscillator Nd:YAG laser. Since the frequency of the laser oscillators is fixed at 30 Hz each, a pulse generator is utilized to fire each lamp at the desired time, and with the required time separation between pulses. The maximum power is rated at 400 mJ per pulse, for the 532 nm wavelength (corresponding to green light), but the actual maximum output power achievable range is from 300 mJ to 350 mJ per pulse. The pulse width is about 7 ns. A sketch of the PIV and optical setup is shown in Fig. 1. This figure also shows the location of the Pt wires.

PIV images are acquired by a high resolution CCD camera. A typical image from a PIV measurement of the two phase boundary layer is shown in Fig. 2. The camera resolution is 10 bits, 1016 $\times$ 1016 pixels, and it runs at 30 Hz. This camera has a 1-in. CCD array format, and the pixel size is 9 μm. The CCD camera also has the trigger double exposure capability, which allows for acquiring two successive frames every 30th of a second. In order to do so, the data acquired during the first CCD array exposure is moved to a transfer array in about 5 μs, and then the CCD array is ready again to acquire new data. The data in the transfer array is sent out to the imaging board. Therefore, correct synchronization must be performed between the CCD camera and the laser system light pulsing. A high accuracy pulse generator performs the synchronization.

The exposure time for the first frame is only 0.128 ms, but for the second frame the CCD array is exposed for 32.4 ms. Thus, the

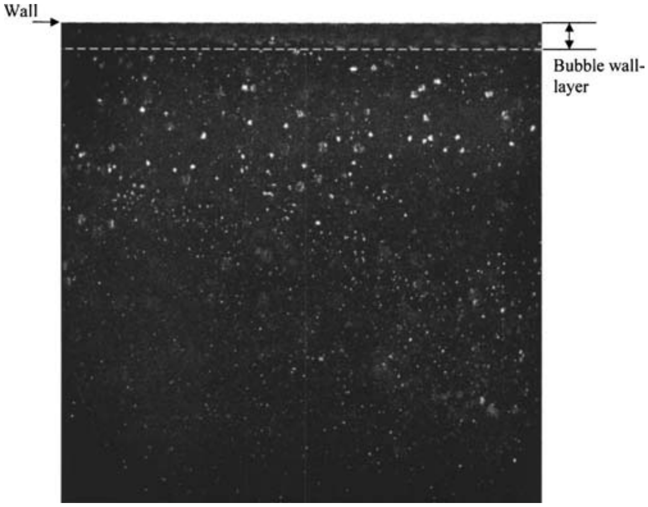

Fig. 2 Typical image from a two phase boundary layer measurement

first laser oscillator must be fired during the first frame exposure, but the second laser light pulse can be fired anytime during the 32.4 ms that the CCD array is again exposed, so that the time interval between two consecutive frames can be set as desired. Clearly, this feature allows studying highly turbulent flows with a high spatial resolution. In this work, the time separation between images used was 1 ms, the view area was set to 1.05 cm^2, and the resolution of the camera was set to 8 bits, 1008×1012 pixels. The velocity field acquisition rate, i.e. two successive frames with a time separation of 1 ms was 30 Hz.

Data Processing

In this study, particle tracking routines based on the cross correlation algorithm were employed. Two different programs were used for particle extraction and tracking process. The resulting velocity vectors from each application were then compared and combined. This hybrid tracking technique greatly increased the total number of velocity vectors used for the flow field analysis. The first software allowed for online image processing and tracking of the particle fluid tracers. Thus, the image threshold and tracking parameters can be easily and correctly set for a whole data set. The particle extraction algorithm is based on the template matching. The template is a one-dimensional pattern with three points, which accelerates the particle detection [17]. The tracking process is a binary correlation method [18]. Label matching and median filter checking are used in a post-processing step to reduce particle mismatching during the tracking process. This program is considered robust and reliable for particle centroid determination and tracking, as proven during the First International PIV Challenge [19]. Recently, this software has been improved. The recent version of the software was tested at our lab with six different synthetic image pairs of a strong vortex with different seeding concentrations. These cases were obtained from the First International PIV Challenge.[3] The number of vectors found with this improved version increased and the root-mean-square (rms) error in pixels was reduced from 0.433 to 0.362 which is about 16.2% reduction in the error. This error reduction was obtained in five out of the six benchmarked cases.

The second particle extraction and tracking program is a home-developed routine by Hassan et al. [20], and it has been improved over the years. The particle centroid determination algorithm uses a two-dimensional mask to determine the area of the particle image, and then a center-of-mass calculation yields the particle image centroid. The border of the spots is determined from the computation of the average gray scale intensities on windows of given dimensions. The influence of the average intensity of the surrounding windows is also taken into account in the calculations. Then, all those pixels with intensities higher than the average plus a standard deviation are kept for the calculations. This allows separating the different particle spot images in each window. The obtained particles are then binarized and labeled for the cross-correlation tracking step. Next, the pixels that belong to the same spot are used for the computation of the centroid. This software was also tested with the same image pairs mentioned above, yielding a lower number of vectors, but similar results to those of the first software with comparable rms error. Another advantage of this software is that the search region can be predetermined. This is particularly important in areas where the particle displacements are small, as in the regions close to the wall. A consistency filter is used to ensure vector quality.

In the tracking process, the flow field PIV images for single- and two-phase flows were divided into multiregions parallel to the channel wall, to resolve the high velocity gradient of the boundary layer. Each image was divided into four strips normal to the y direction with an optimum thickness for the tracking process. Determining the optimum thickness is to have a lesser number of regions to accelerate the tracking process, while ensuring that the magnitude and direction of the velocity vectors are consistent within the region. Figure 3 shows a vector velocity field composed of 40 instantaneous, consecutive, velocity fields. This figure also shows the four regions used for the particle tracking, and the velocity profile obtained once the whole data processing was complete. The region thicknesses for this case were chosen to be $\Delta y = 1.1$ mm, 2.1 mm, 5.7 mm, and 1.6 mm, for regions 1, 2, 3, and 4, respectively.

Once the velocity vectors are obtained from both particle tracking algorithms, they undergo a filtering process. The filters are applied independently to the vector data sets from each tracking process. The first filter is related to a specified cross correlation value. In our case, to achieve high accuracy in velocity vectors, only those vectors with a cross correlation coefficient value higher than the average value of a whole vector data set are considered in the flow field analysis. During this step usually about 50% of the total vectors are removed. Next, neighbor and consistency filters were applied. Some of the vectors can easily be determined as erroneous vectors. These vectors were with direction and/or magnitude far deviated from the neighbors. The filters' function is to remove vectors that are not within the average +/− a standard deviation value of the magnitude and direction of the representative velocity vector in a small window. This step ensured that velocity gradients were continuous along the x and y directions. Then, those vectors close to the image boundaries are also removed. In this step about 10% of the vectors are removed. In total, only about 40% of the initially tracked vectors were kept for the flow analysis after the filtering process. The remaining vectors from each process are combined to one single file, where they are compared to remove repeated vectors.

Once the velocity vectors from the hybrid-tracking scheme are filtered, all the instantaneous velocity fields $\mathbf{U}=\mathbf{U}(U,V)$ are added in a single data file. Then, mean velocity $\bar{\mathbf{U}}=\bar{\mathbf{U}}(\bar{U},\bar{V})$ and fluctuating velocity $\mathbf{u}=\mathbf{u}(u,v)$ fields are calculated. The Reynolds decomposition relation was used here to obtain the fluctuating velocity field, i.e.; $\mathbf{u}=\mathbf{U}-\bar{\mathbf{U}}$.

Finally, the velocity vector accurate positions from the wall are determined. This y coordinate, from the wall, is important in the computation of the wall friction velocity.

Single-Phase Boundary Layer Measurements

In this study, the single-phase measurements consisted of ten image data sets. Each set was composed of 100 consecutive 1008×1012 pixel, 8-bit images. Thus, a total of 500 velocity

[3]www.pivchallenge.org

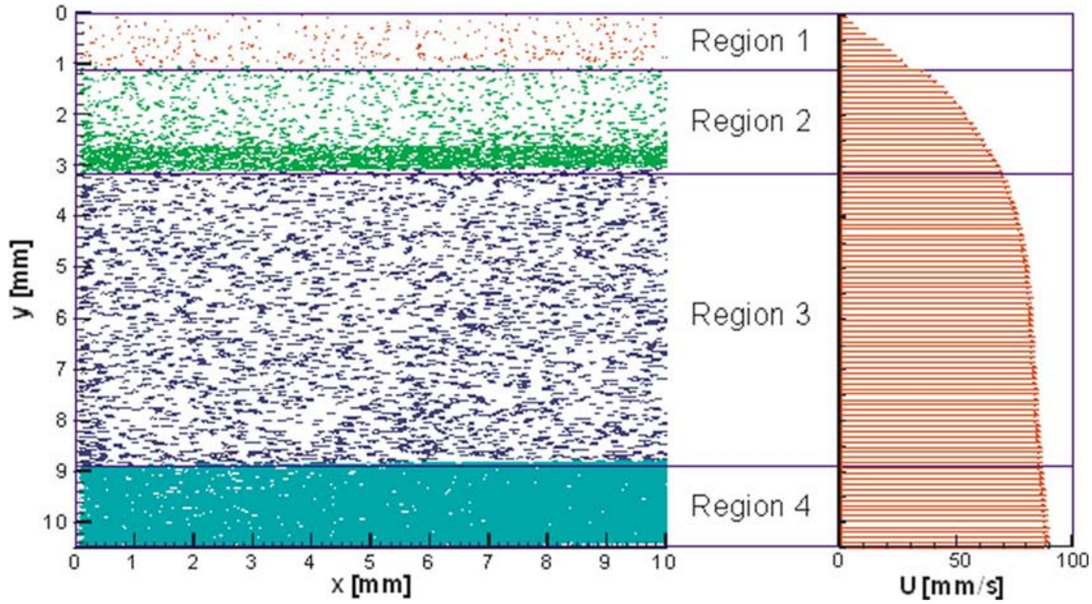

Fig. 3 Overlay of the velocity vectors from 40 consecutive instantaneous fields, and final velocity profile after dividing the velocity field into multiregions for optimum tracking

fields were obtained. However, because not all the images satisfied the minimum quality necessary for image processing, about 450 velocity fields were used for the final data analysis. The mean cross-sectional velocity was 7.72 cm/s. The Reynolds number Re based on the half height of the channel H is 3400. Based on the hydraulic diameter, Re was 8570. The measurement zone was located at $L/2H=23.34$.

Single-phase velocity vectors, of an average of 59,434 vectors per data set, were used to calculate the mean velocity profile along the y direction, within the measurement zone. Each point on the velocity profile was computed by averaging all the velocity vectors that fall in region sheets of 1008×20 pixels, with 50% overlapping. Two main issues are related to choosing the suitable grid size for the ensemble average. First, it has enough data points on the mean velocity profile to compute the friction velocity. Second, the total number of vectors, used for the calculation of the average velocity vector at each point of the velocity profile should be at least the required minimum samples for achieving reliable statistics. Regarding the number of vectors required for the ensemble average, it was considered that about a 1000 velocity vectors per strip is appropriate for the averaging process. This was, however, not achievable for some of the microbubble laden flow data sets; particularly, high void fraction sets. Taking into consideration that not all of the strips could have the minimum vector quantity required, it was determined that at least 20 data points were required to satisfactorily compute the friction velocity from the mean velocity profile. For the reasons just discussed, it was concluded that region sheets of 1008×20 pixels sizes were appropriate.

From the average of the ten mean velocity profiles, one from each data set, it was determined that the boundary layer size δ was about 7.5 mm. This is based on the premise that at such a position the mean velocity reached 99% of the velocity outside the boundary layer, i.e.; $\delta_{99}\approx 7.5$ mm. The external velocity was considered to be the mean cross-sectional velocity. Point statistics for the mean and turbulence quantities were calculated with the total number of instantaneous velocity vectors, which was 594,344 vectors, assuming homogeneous flow in the streamwise direction.

Wall Friction Velocity

Friction drag reduction measurements require that the wall shear stress τ_w is either directly measured or calculated from the pressure drop. Once τ_w is known, the skin friction coefficient C_f for the cases of drag reduction and without drag reduction can be compared. C_f is calculated from

$$C_f = \frac{\tau_w}{\frac{1}{2}\rho u_m^2} \tag{1}$$

which is equivalent to

$$C_f = 2\left(\frac{u_\tau}{u_m}\right)^2 \tag{2}$$

where ρ is the liquid density, and u_τ is the wall friction velocity. For low Re, the pressure drop in a short distance requires very high accuracy differential pressure transducers, which are not easily commercially available and are expensive. Moreover, the uncertainty of such differential pressure transducers is of the same order of the required measurements. The use of hot film probes or hot wires is common for the measurement of wall shear stress, but they may induce disturbances to the flow, especially close to the wall. Another problem related to the use of pressure transducers, hot wires, or hot films is that the presence of high voltages contaminates the actual sensor signal. In our particular case, these kinds of sensors could not be employed because of the high voltage used for the electrolysis process, which introduced high intensity noise. Thus, it was not possible to discriminate noise from the actual signal of the pressure transducers. The height of the water column at different streamwise positions showed no reliable measurable difference either.

The PIV technique, and its derivative PTV in our case, allows measuring the velocity field at regions close to the wall. From these measurements u_τ can be determined, since in the viscous sublayer $u^+=y^+$. Here u^+ and y^+ are the velocity and the normal distance from the wall normalized with near-wall scales. However, it is necessary to determine the limit of the viscous sublayer ($y^+=5$) region, which is the distance from the wall, in physical coordinates, that transition from the viscous layer to the buffer zone occurs. Therefore, a rough estimation of u_τ needs to be obtained, and then, the data points that fall in the viscous sublayer can be used to determine the best estimate of u_τ value.

In this study, three approaches are performed to evaluate u_τ value: namely, from the Blasius equation, power law, and Durst et al. method.

For flow in conducts, the Blasius equation for the friction factor can be used to calculate u_τ as a first approximation, since C_f is a function of Re. For channel flow, the relationship between C_f and Re is given by

$$C_f = 0.073\mathrm{Re}_m^{-1/4} \tag{3}$$

where Re_m is the Reynolds number based on the mean flow, that is,

$$\mathrm{Re}_m = \frac{2Hu_m}{\nu} \tag{4}$$

where ν is the kinematic viscosity of the liquid.

Another option to approximate the trial of u_τ is to use the power law form for the mean velocity distribution, instead of the traditional Law of the Wall, of a turbulent boundary layer

$$u^+ = Cy^{+\alpha} \tag{5}$$

In this case, for channel or pipe flow, u_τ can be computed from [21]

$$u_\tau\frac{d}{\nu} = \left[\frac{\mathrm{Re}_m 2^\alpha \alpha(1+\alpha)(2+\alpha)}{\sqrt{3}+5\alpha}\right]^{1/(1+\alpha)} \tag{6}$$

where

$$\alpha = \frac{3}{2\ln \mathrm{Re}_m} \tag{7}$$

and d is the pipe diameter or the channel height. The value of C in Eq. (5) is calculated from

$$C = \frac{\sqrt{3}+5\alpha}{2\alpha} \tag{8}$$

The main problem in calculating u_τ from velocity measurements in the viscous sublayer is that very few data points can be obtained, and the measurement uncertainty can be high, due to closeness to the wall. To avoid this problem, Durst et al. [22] have proposed an alternative method to estimate u_τ. This method allows using points up to a distance $y^+=12$ and therefore more data points can be used to determine u_τ. This method consists of expanding the fluctuating components of the velocity vectors in a Taylor series to approximate the Reynolds stress in the near wall region. This approximation is substituted into the momentum equation. Then, u_τ and the distance to the wall correction y_0 are computed from the solution to the polynomial using least-squares fitting (Eq. (9)).

$$\bar{U} = \frac{u_\tau^2}{\nu}(y-y_0) - \frac{u_\tau^2}{2R\nu}(y-y_0)^2 + D(y-y_0)^4 + E(y-y_0)^5 \tag{9}$$

In Eq. (9), R is the pipe diameter or the channel half height H. The parameters D and E have insignificant contribution, so they can be either included or ignored in the computations of u_τ. Our experience indicates that these two parameters slightly improve the final result of u_τ. If they are not considered in the computations, it will generally require more iterations to reach the same final value of u_τ. The wall correction y_0, on the other hand, can be used as free parameter to accelerate the calculations and improve results. The y_0 parameter can be obtained with high accuracy during the image calibration where the channel wall can be accurately determined, either before or after the experiments. Since y_0 is considered already known, and D and E can be ignored, consequently, Eq. (9) reduces to

$$\bar{U} = \frac{u_\tau^2}{\nu}y - \frac{u_\tau^2}{2R\nu}y^2 \tag{10}$$

which is equivalent to

$$\bar{U}^+ = y^+ - \frac{1}{2R^+}y^{+^2} \tag{11}$$

where

$$R^+ = \frac{Ru_\tau}{\nu} \tag{12}$$

is the dimensionless pipe radius, and is replaced by nondimensional channel half height H^+ for channel flows.

To achieve a first approximation of u_τ, the Blasius equation or the power Law can be used. Iterations for each point that satisfies $y^+ \leqslant 12$ are performed using Eqs. (11) and (12), until u_τ converges. Finally, an average value of u_τ can be calculated. Figure 4 shows a comparison of the nondimensional velocity profile, obtained from the average of all ten single phase data sets, using u_τ from each of the methods described above. It also includes the Law of the Wall and the power law profiles. In this figure, Durst, Blasius, and power, refer to the u_τ value used for the calculation of the wall variables, computed from each respective method. Clearly, the Durst et al. method shows the best agreement with both the Law of the Wall and the power law in the log region. Therefore, we selected the Durst et al. method for the calculation of u_τ. The Law of the Wall is given here by Schlichting and Gersten [23]

$$u^+ = y^+ \quad 0 \leqslant y^+ < 5 \tag{13}$$

for the pure viscous sublayer

$$u^+ = \frac{1}{\Lambda}\left[\frac{1}{3}\ln\left(\frac{\Lambda y^+ + 1}{\sqrt{(\Lambda y^+)^2 - \Lambda y^+ + 1}}\right) + \frac{1}{\sqrt{3}}\left(\arctan\left(\frac{2\Lambda y^+ - 1}{\sqrt{3}}\right) + \frac{\pi}{6}\right)\right] + \frac{1}{4\kappa}\ln(1+\kappa B y^{+^4}) \quad 5 < y^+ < 70 \tag{14}$$

where $\kappa=0.41$, $A=6.1\times10^{-4}$, $B=1.43\times10^{-3}$, $\Lambda=(A+B)^{1/3}=0.127$ for the buffer layer; and finally for the overlap or logarithmic layer

$$u^+ = \frac{1}{\kappa}\ln(y^+) + C^+ \quad y^+ > 70 \tag{15}$$

where

$$C^+ = \frac{2\pi}{3\sqrt{3}\Lambda} + \frac{1}{4\kappa}\ln(\kappa B) = 5.0 \tag{16}$$

In our case, we did not reach the overlap layer in any of our measurements. In this case, the power law is given by

$$u^+ = 7.60y^{+^{0.170}} \tag{17}$$

The Law of the Wall approach better described our measurement data within the boundary layer. It is known that the power law is not valid in the region $y^+ \leqslant 30$, as also confirmed in Fig. 4. It has also been argued that the Law of the Wall is not valid in the same region; however, our data show a reasonable agreement.

Two-Phase Boundary Layer Measurements

The microbubbles were generated at a distance of 1 cm from the top wall. The measurement zone was about 35 cm from the Pt wire position. Prior to the PIV measurements, images of the bubbles generated via the electrolysis process were taken. From these images, and using the Pt wire diameter (76 μm) size as reference, the microbubble diameter was determined, at different liquid flow rates. About 60% of the generated microbubbles had a diameter less or equal to 40 μm at a liquid velocity of 10 mm/s, with two main peaks at 26.6 μm and 30.4 μm, as shown in Fig. 5. This study involved a higher flow rate. Consequently, the expected microbubble size generated by electrolysis had a peak less

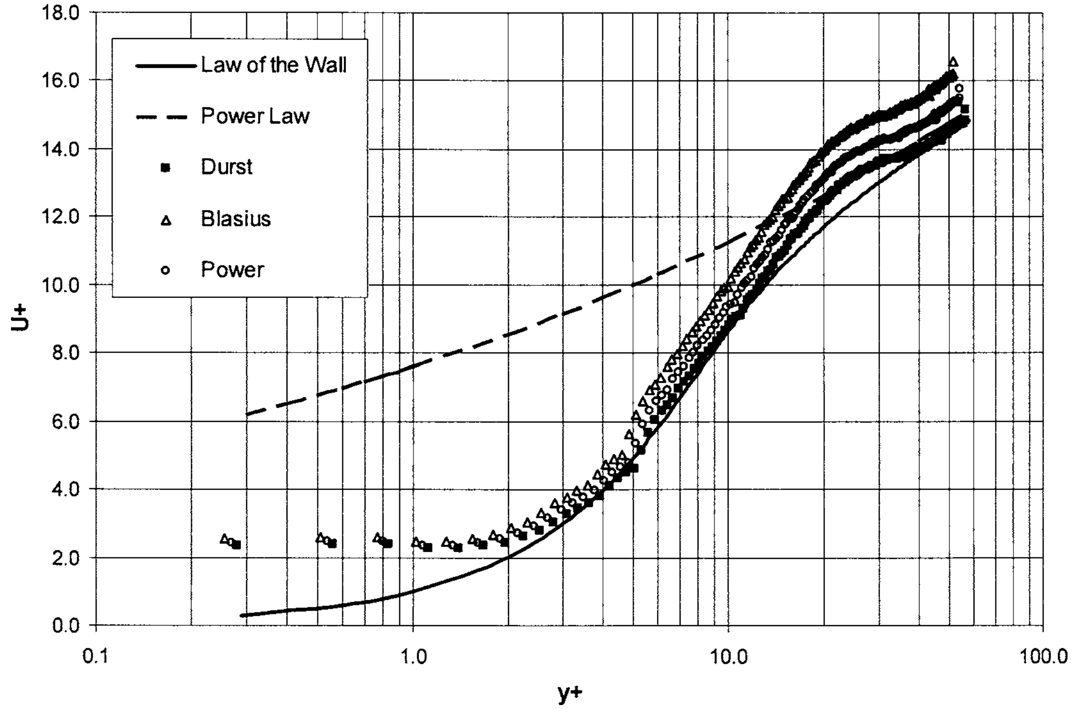

Fig. 4 Comparison of the mean velocity profile in the single phase boundary layer, using the three different methods shown to compute the wall friction velocity

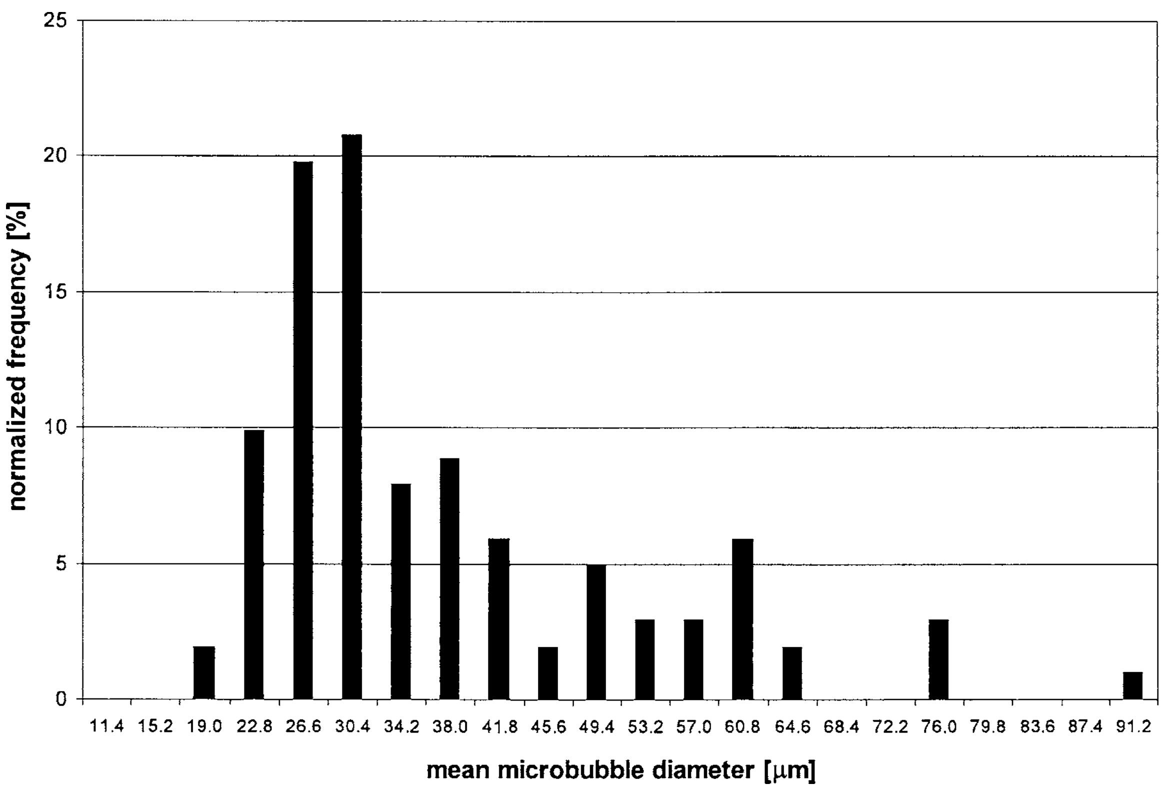

Fig. 5 Microbubble size distribution at a liquid velocity of 10 mm/s

than 30 μm. Ten image data sets of the microbubble laden flow were acquired at the same liquid flow rate in the single-phase flow test case. Due to the buoyancy, microbubble accumulation occurred at the top wall. This can be seen at the upper part of the image in Fig. 2, and thus resulting in an increase of the void fraction in the measurement volume. An average of 45 velocity fields (90 frames) were obtained from each data set. The average number of vectors per data set was above 70,000.

In several experimental studies, it is indicated that the drag reduction increases as volumetric bubble concentration, β increases, until a maximum value of the drag reduction is reached [1,5,6]. No increase in the drag reduction was observed beyond

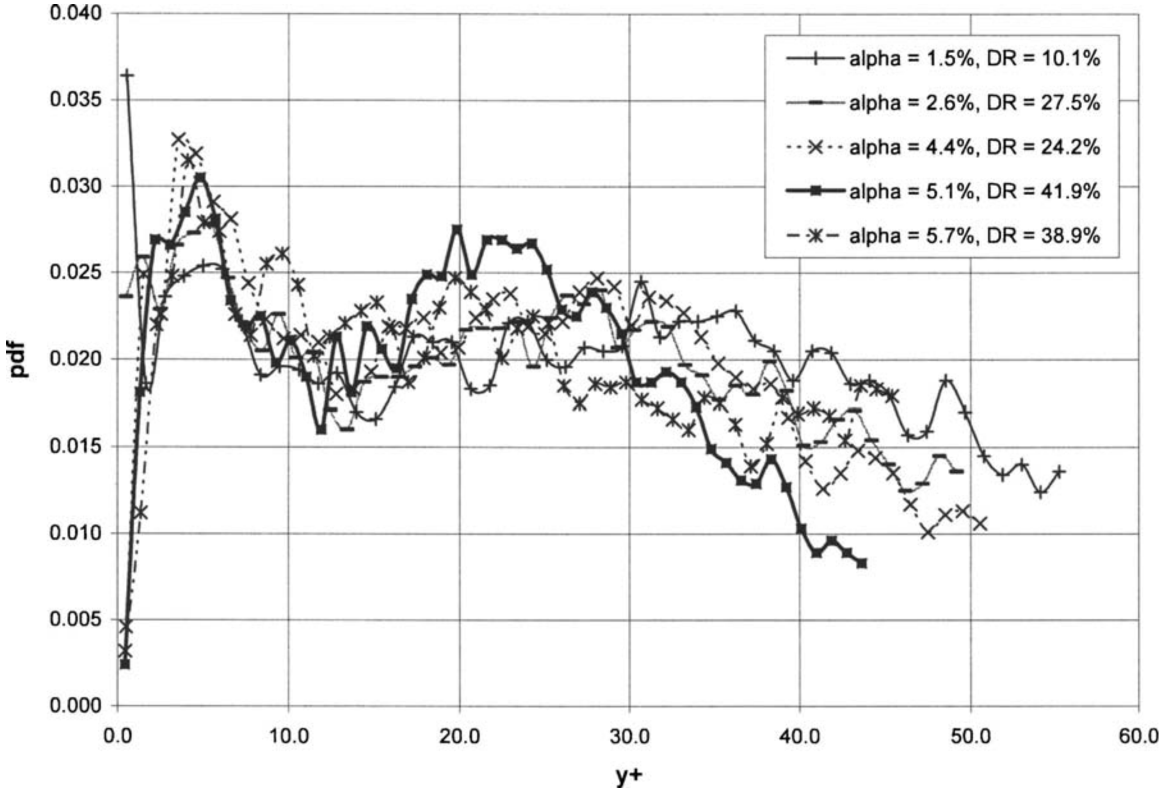

Fig. 6 Distribution of the freely moving microbubbles in the boundary layer, for five different drag reduction values

this value during the increase in β. Drag reductions as high as 80% were achieved with a value of $\beta=25\%$, reported by Fontaine et al. [6]. However, β was about 40% in the study of Madavan et al. [5] for the same 80% drag reduction gain. Note that two different geometries were employed in the mentioned studies, but similar definitions for the volumetric liquid flow rate Q_l were used. However, since void fraction α is not necessarily equal to β, a correlation between α and drag reduction is not clear at present time.

In principle, both size and spatial distribution of the microbubbles are obtained from PIV data. The distinction between particle fluid tracers and microbubble images was performed using both the area and brightness of the image spots. Microbubble images have larger area and higher gray level than the tracer images. In this study, low local void fractions were produced, i.e., less than 5%. Such low void fractions allow the use of the PTV technique for the velocity field measurements of both dispersed and continuous phases. Although the microbubble production rate was kept constant during all the measurements, there was microbubble accumulation at the channel top wall. The thickness of this bubble layer at the top wall depends on the liquid velocity for each different test. In this study, the total void fraction in the measurement volume was calculated by adding the contribution of the top wall bubble layer plus the freely flowing microbubbles within the viewing volume, that is

$$\alpha = \alpha_{\mathrm{bl}} + \alpha_{\mathrm{fb}} \tag{18}$$

where α_{bl} is the void fraction of the layer of accumulated microbubbles at the channel top wall (wall-bubble layer), and α_{fb} is the void fraction due to microbubbles that transport with the flow (free bubble). The first part of α was computed assuming that the bubble layer occupied volume of a rectangular box V_{bl}, that is,

$$V_{\mathrm{bl}} = l \times b \times h, \tag{19}$$

where l is the image size along the x direction (1008 pixel $=10.54$ mm), b is the laser light sheet width ($\sim$1 mm), and h is the bubble layer thickness which accumulated at the top wall. This parameter h varied from 15 to 63 pixels, and thus, α_{bl} varied from 1.5% to 6.2%. Particularly, the second contribution α_{fb} did not change, in practice, during the experiment under same flow condition. A maximum of 300 microbubbles was found on the images representing the contribution of α_{fb}. Therefore, the value of α is close to the value of α_{bl}. However, the distribution of the freely moving microbubbles in the boundary layer (α_{fb} distribution) was proved to be a key parameter in achieving the drag reduction. In this study, it is found that the local distribution and profile of α_{fb} in the boundary layer have paramount influence on the drag reduction.

Figure 6 shows the α_{fb} distribution versus y, the normal distance from the wall, for five different two phase microbubble/water data sets. The void fraction values shown in the figure are for the total value of α within the viewing volume. It can be noted that the different data sets do not have a common initial point. This reflects the thickness of the microbubble layer at the top of the channel wall. Also, these profiles do not start at a value of zero; however, the number of microbubbles at the initial point is small. In these data sets, the distribution clearly indicates two peaks. The first peak appears just after the bubble layer ($y^+\sim 5$), and the second peak at about the middle of the measurement area ($y^+\sim 25$). The first peak is quite narrow compared to the second one, in which a gradual increase and decrease can be seen. It is also noted that the maximum value of α of 5.7% does not corre-

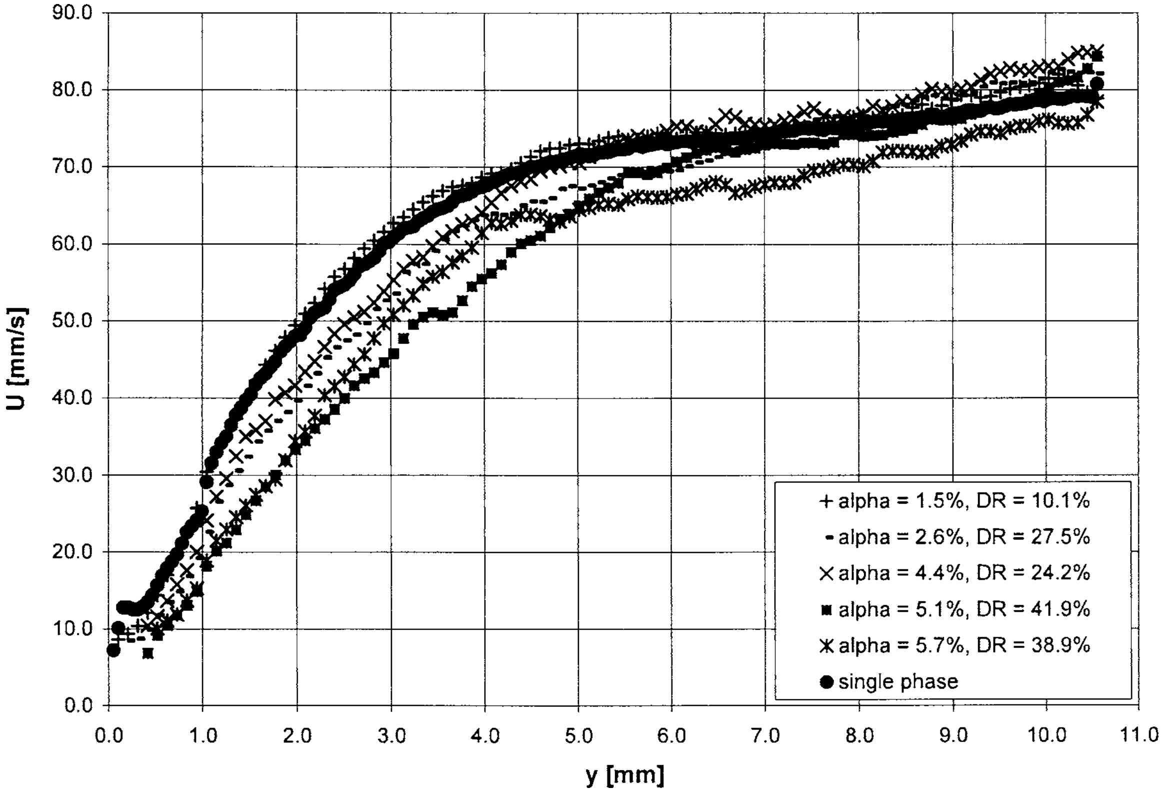

Fig. 7 Modification of the profiles of the streamwise component of the liquid mean velocity vector across the two phase boundary layer, for five different drag reductions, in physical coordinates

spond to the highest peaks at $y^+ \sim 25$. Beyond a distance of about 10 mm from the wall, the bubble distribution rapidly falls towards zero.

Drag Reduction Results

In this study, the drag reduction was calculated based on the measurements of the wall friction velocity u_τ. To calculate the drag reduction (DR) we use the ratio of the skin friction coefficient of the microbubble laden turbulent boundary layer C_f to the skin friction coefficient of the liquid single-phase turbulent boundary layer C_{f0}. This ratio is equal to the ratio of the wall shear stress of the microbubble/water flow τ_w to the wall shear stress of the single liquid flow τ_{w0} case. Thus, using Eq. (2), the percent drag reduction was calculated from

$$\mathrm{DR} = 100 \times \left[1 - \left(\frac{u_\tau}{u_{\tau 0}}\right)^2\right] \tag{20}$$

It is known that an increase in the void fraction in the boundary layer leads to an increase in drag reduction, until a maximum value is reached. In this study, the magnitude of local microbubble void fraction in the buffer zone is found to be the key parameter in drag reduction. The stagnant bubble layer at the top of the channel wall has practically insignificant effect on the drag reduction. Figure 6 shows that the first peak of the microbubble PDF, which is located in the viscous sublayer, does not play an important role in the drag reduction phenomenon. In addition, Fig. 6 indicates that although the void fraction profiles are similar, those profiles with microbubble accumulations within the zone from $y^+ \approx 15$ to 30 achieve higher drag reductions. For example, the case of $\alpha = 5.1\%$ yields higher drag reduction than the case of $\alpha = 5.7\%$. This is due to a higher local void fraction within this critical zone ($y^+ \approx 15$ to 30) for the case of $\alpha = 5.1\%$. By injecting more microbubbles, the probability of obtaining more bubbles in the buffer zone increases. This is the first time, to our knowledge, that present experimental local information confirms that high percentage drag reductions can be achieved with very low local void fractions, once they are within the critical zone.

Figure 7 shows the effect of the void fraction on the streamwise component U of the liquid mean velocity distribution across the normal distance from the wall. With larger values of the microbubble void fraction in the critical zone (see Fig. 6), smaller velocity gradients near the wall are obtained. This figure clearly shows a decrease of the slope dU/dy as drag reduction reaches higher values. It is an indication of the thickening of the viscous layer. It is interesting to note the close similarity of velocity profile, and drag reduction, produced with two quite different values of void fraction, $\alpha = 2.6\%$ and $\alpha = 4.4\%$. However, the microbubble accumulation within the critical zone, $y^+ \approx 15$ to 30, has practically the same values, as shown in Fig. 6. This again confirms that the α_{fb} distribution is a paramount parameter in the drag reduction phenomenon by microbubble injection in the boundary layer.

The velocity profiles shown in Fig. 7, normalized by the wall friction velocity, are presented in Fig. 8. Note in this figure that the viscous sublayer grows up to a distance of $y^+ \approx 12$ (compared to the limit $y^+ = 5$ for single phase) for the higher drag reduction cases. The log-law region is retained, but it is displaced upward and parallel to the single-phase case. A similar behavior is obtained with surfactants and polymers [24,25]. Increasing the local void fractions within the critical zone deviates more from the single phase flow law of the wall in the buffer and logarithmic regions, as clearly shown in Fig. 8. The figure further indicates that the data, for the obtained different drag reduction cases, follow closely the curve $u^+ = y^+$ up to $y^+ \approx 12$. Then, they tend to preserve a profile closer to linear, in the log scale, than the single phase case up to $y^+ \approx 20$, where the log-law profile starts becoming apparent. It is clear that the transition from the modified buffer to log-law regions is not as smooth as it usually develops for the single phase flow cases.

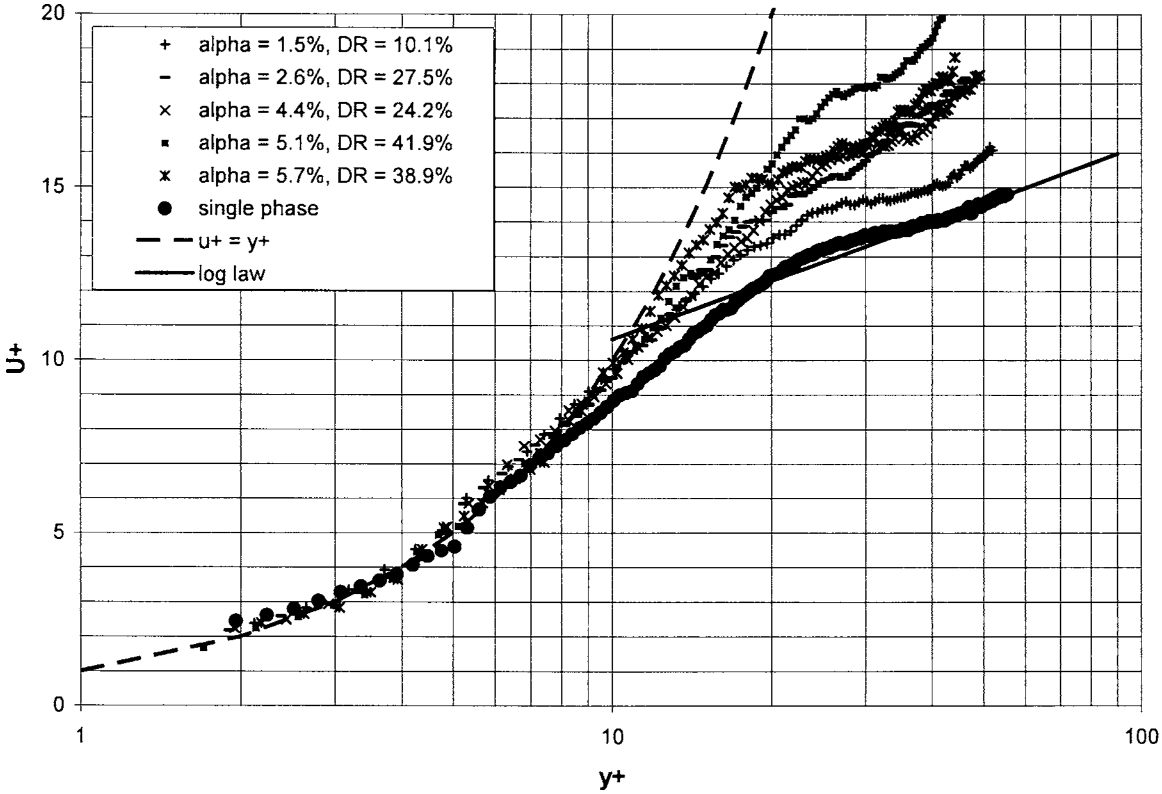

Fig. 8 Modification of the profiles of the streamwise component of the liquid mean velocity vector across the two phase boundary layer, for five different drag reductions, in wall coordinates

To explain the drag reduction phenomenon, Xu et al. [3], from their numerical simulation results, suggested three mechanisms involved: the initial seeding location of microbubbles, density effects, and specific correlations between microbubbles and liquid turbulence. The increase of drag reduction with increasing void fraction has been reported, and the modification of the turbulence in the boundary layer was also measured. In this work, it is also shown that the location of the microbubbles is a key parameter in the description of the phenomenon. One way to address the buoyancy influence in the microbubble drag reduction is to determine the modification of the normal component of the liquid mean velocity vector V across the boundary layer with various drag reductions and/or the void fraction magnitudes. Figure 9 demonstrates this effect. It is clear that for the high drag reduction case (41.9%), V is moving away from the wall (positive direction). On the contrary, the lowest drag reduction case shows a tendency to move toward the wall. The rest of the cases are not shown to avoid overcrowding the figure. However, similar trends are obtained, i.e., normal velocity components of liquid phase are positive (away from the wall) with high drag reduction, and moving toward the wall for low drag reduction ($DR < 20\%$). It should be mentioned that the bulk velocity in this experiment was low. Figure 9 indicates that the buoyancy effect only cannot explain completely the drag reduction phenomenon. Ferrante and Elghobashi [14] concluded, from their numerical simulation results, that the drag reduction was caused almost entirely by a velocity divergence effect, associated with the void fraction, since the presence of microbubbles generated a local positive divergence of the fluid velocity, creating a positive mean velocity normal (and away from) the wall.

All the cases investigated by Ferrante and Elghobashi show the positive divergence of the fluid velocity. However, the data, in Fig. 9, for the case of lowest drag reduction (10.1%) shows V going toward the wall (negative direction), while in the 27.5% and 24.2% cases (not shown in the figure) the data points spread noticeably between the trend lines. Although this could be a consequence of the high uncertainty of this velocity component, considering its small magnitude, it also indicates that a threshold value for the void fraction is required, for the velocity gradient effect to occur. Figure 9 can also be used to estimate the error of the normal velocity component. This can be deduced from the average normal velocity profile for single liquid phase flow test. The mean error value was −0.24 mm/s, with a standard deviation of 0.23 mm/s. It is clear from the figure that the error reduces as moving farther from the wall. If the error for each of the four tracking segmented regions as illustrated in Fig. 3 is considered, the rms error of the normal velocity component is 0.42 mm/s, 0.30 mm/s, 0.11 mm/s, and 0.08 mm/s, for regions 1, 2, 3, and 4, respectively. The first two values of the rms error are higher than those computed from the error propagation formula, as it will be shown in the measurement uncertainty section. It is clear that better resolution of the normal velocity components near-wall region is required.

Vorticity fields were derived from the measured velocity fields for the single- and two-phase flow cases. The spanwise z component of the mean vorticity field was computed with central finite differences, from the measured velocity fields of the continuous phase. In this calculation, the velocity fields were divided into regions of 60×60 pixels, with 50% overlapping. The vorticity results showed a similar finding of drag reduction by polymer and surfactant injection [25,26]. Regions of high vorticity decrease as drag reductions increase. Figures 10–12 show the z component of the mean vorticity field for three different drag reduction cases of 10%, 27.5%, and 41.9%, respectively. The single-phase vorticity field is about the same as the case of 10% drag reduction. The reduction of vorticity magnitude occurs close to the wall as the drag reductions increases. It indicates that microbubble/turbulence interactions occur in the buffer zone, leading to a destruction of vorticity structures within the transition region from viscous to the buffer zone. These results plus the findings related to the modifi-

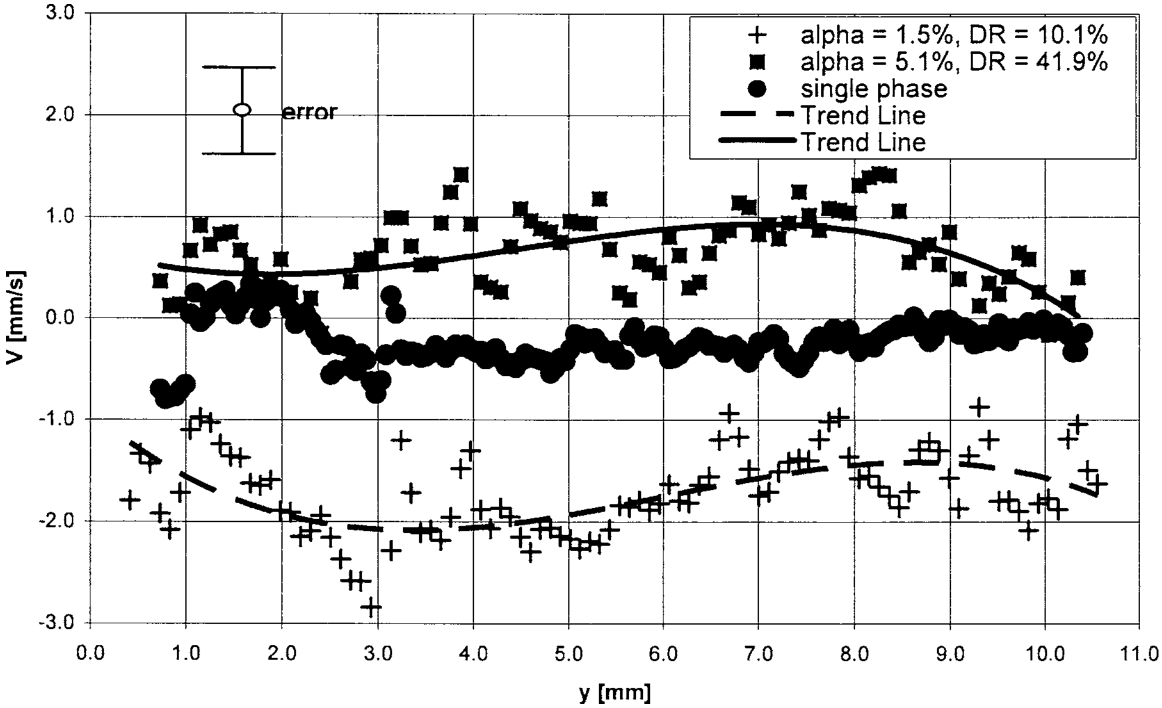

Fig. 9 Modification of the profiles of the normal component of the liquid mean velocity vector across the two phase boundary layer, for the highest and lowest cases of drag reduction, in physical coordinates

cation of the components of the mean velocity vector infer that drag reduction by microbubble injection is not a simple consequence of density effects only.

Measurement Uncertainty

The uncertainty in the velocity measurements obtained using PTV is a direct consequence of a combination of errors from two main sources. These are the localization of the centroid of the seed particle and microbubble images and their displacements in the two-dimensional (2D) images, and the uncertainty of how well the tracer particles follow the actual fluid motion. This last uncertainty can be determined utilizing the particle Stokes number, which is calculated as the ratio of the relaxation time of the seed particle to the characteristic time of the flow. The particle relaxation time τ_p, also known as the momentum or velocity response time, is the time needed by a seed particle to reach the value $e^{-1}U$, if the particle was initially at rest. Here U is the fluid velocity. The time τ_p can be computed from

$$\tau_p = \frac{(2\rho_p + \rho_f)d_p^2}{36\mu_f} \tag{21}$$

where ρ is the density, d the seed tracer diameter, μ the viscosity, and the subscripts p refers to particle properties, and f to the fluid properties. In this experiment, $\rho_p = 1050\ \text{kg/m}^3$, $\rho_f = 1000\ \text{kg/m}^3$, $d_p = 6 \times 10^{-6}$ m, and $\mu_f = 1002 \times 10^{-6}\ \text{kg/(m s)}$. Thus, the relaxation time of the seed was calculated to be 3.0 μs.

The fluid time scale τ_f is the time needed by the fluid to be advected within a characteristic length L, at a velocity U, that is

$$\tau_f = \frac{L}{U} \tag{22}$$

To compute the characteristic time of the flow, the seed tracer mean diameter and the average cross-sectional velocity of the liquid were used. The resultant fluid time scale is 77.7 μs. Then, the resulting Stokes number τ_p/τ_f is 3.9×10^{-2}. Therefore, the 6 μm seed particles closely followed the fluid motion changes, and therefore did not significantly contribute to the total error.

The major source of error in this experimental investigation is the uncertainty in determining the centroid of the spot images of both the tracer particles and microbubbles. The error in locating the centroid displacements depends on the optical parameters of the camera, lenses, laser, and the algorithm for finding the particle-image centroid. As mentioned before, two different software applications were used for spot centroid finding and particle tracking. In both cases, the centroid is computed using the center-of-mass location method, by weighing every pixel with the value of its intensity, that is, if $I(x,y)$ is the gray scale pixel intensity at the position (x,y) on an tracer seed particle or microbubble spot image, the center-of-mass location is given by

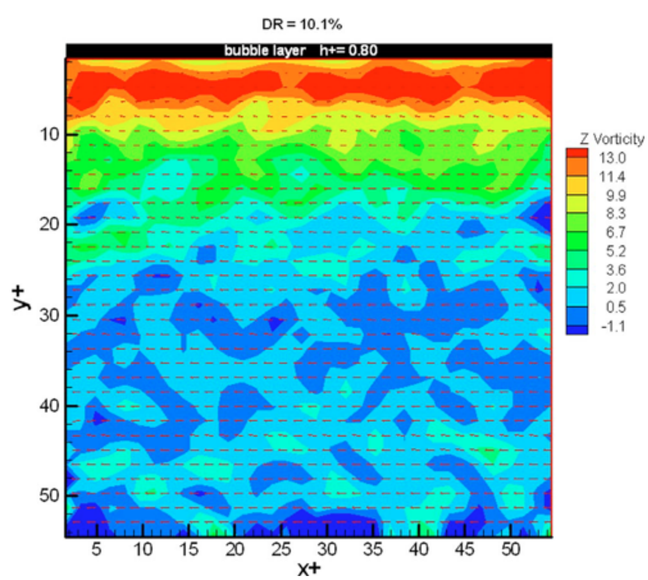

Fig. 10 *z* component of the mean vorticity field for the drag reduction of 10.1% case

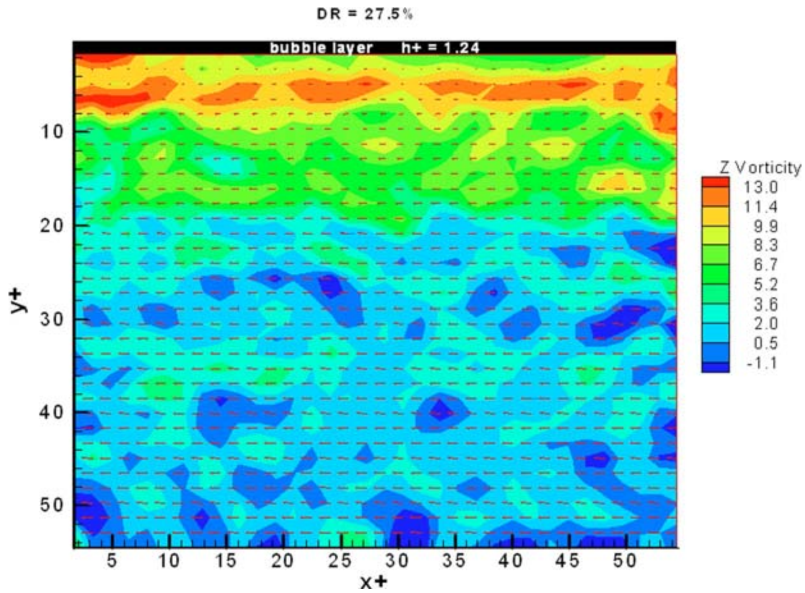

Fig. 11 ***z*** **component of the mean vorticity field for the drag reduction of 27.5% case**

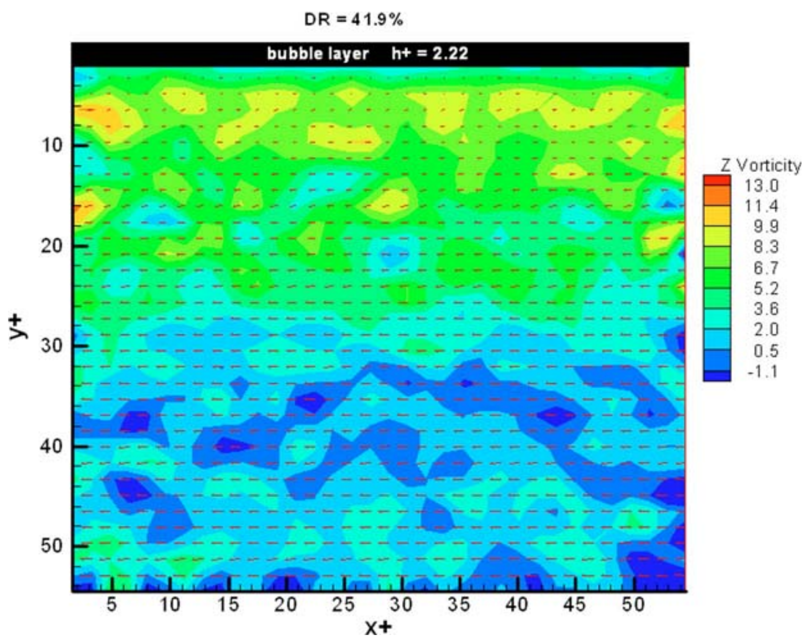

Fig. 12 ***z*** **component of the mean vorticity field for the drag reduction of 41.9% case**

$$(x_0,y_0)_{\text{center-of-mass}} = \frac{\sum_{\text{spot area}} (x,y) \times I(x,y)}{\sum_{\text{spot area}} I(x,y)}. \qquad (23)$$

The centroid in this case is called the first-order moment. This algorithm requires a precise determination of the spot image border. This kind of algorithm has typical errors smaller than 0.01 pixel for simulated ideal particle images [27]. However, the error increases as the noise increases and the spot image size decreases. By applying image calibration, a rms error of 0.1 pixel in calculating the particle image centroids was determined. Using the tests of the PIV Challenge [19], it was found a rms error of 0.4 pixel for the displacement on two consecutive frames, for the homemade software application. This error was assumed as the overall error of the measurements, although the other algorithm had a small rms error of 0.25 pixel.

The uncertainty of the components of the velocity vector can be computed through the error propagation formula. This relationship assumes that if the errors associated to a measurement are small and symmetric around zero, the uncertainty associated to any quantity σ_s derived from, for example, three measurements is given by

$$\sigma_s^2 = \left(\frac{\partial s}{\partial r_1}\right)^2 \sigma_{r1}^2 + \left(\frac{\partial s}{\partial r_2}\right)^2 \sigma_{r2}^{2\prime} + \left(\frac{\partial s}{\partial r_3}\right)^2 \sigma_{r3}^{2\prime} \tag{24}$$

where r_1, r_2, and r_3 are the values of the measurements, and σ_{r1}, σ_{r2}, and σ_{r3}, are their respective associated errors. Thus, to calculate the uncertainty of the components of the instantaneous velocity vectors $\mathbf{U}=\mathbf{U}(U,V)$, we first note that the velocity components are calculated from the subtraction of the coordinates of the position vector $\mathbf{X}=\mathbf{X}(x,y)$ divided by the time interval between laser pulses Δt. Thus, using Eq. (24), the rms error value of 0.4 pixel implies an error of 0.28 pixel in the calculation of the particle image centroids for the two particle images needed in calculating the displacement. In terms of velocity units, the rms error is then 4.18 mm/s for each velocity component. This value is determined considering negligible error in the time separation between frames (1 ms), and the 0.4 pixel error of the particle image displacement. Although 4.18 mm/s seems a high value, only the first two or three grid points along the y direction had velocity values lower than 10 mm/s. The percentage rms value with respect to the average velocity in the channel is about 5.4%.

The friction velocity u_τ was computed from the average value of the U component at each different y position. Therefore, the uncertainty of u_τ relates to that of $\bar{U}$, which, in turn, comes from the error of the instantaneous values of U. The uncertainty σ associated to the components of the mean velocity vector $\bar{\mathbf{U}} = \bar{\mathbf{U}}(\bar{U},\bar{V})$ can be calculated, using again Eq. (24), from

$$\sigma_{\bar{U},\bar{V}} = \frac{\sigma_{U,V}}{\sqrt{n}} \tag{25}$$

where n is the total number of samples employed in the average calculation. The value of n was 1000, except for about the first four or five grid points, out of at least 21 grid points used in the computation of u_τ, as previously indicated. Thus, $\sigma_{\bar{U},\bar{V}} = 0.13$ mm/s. This is a top value for the uncertainty in the calculation of u_τ. Finally, the maximum calculated error of the drag reduction is about 6.9%, i.e., $\sigma_{\mathrm{DR}}=6.9\%$.

For the vorticity uncertainty, using again the error propagation formula, it can be shown that $\sigma_{\omega z}=\sigma_{\bar{U}}/\Delta x$. Now, since there were at least 100 velocity vectors in each grid point, $\sigma_{\bar{U},\bar{V}} = 0.42$ mm/s and $\Delta x=0.63$ mm, $\sigma_{\omega z}=0.67$ Hz.

The total void fraction was considered to have contributions of a bubble layer formed at the top wall of the channel, plus the microbubbles freely flowing in the view volume. Practically $\alpha = \alpha_{\mathrm{bl}}$ as is estimated from Eq. (18). Thus, it is considered that the uncertainty in the calculation of α_{fb}, σ_{fb}, can be neglected in the calculation of the total error associated with α. To determine the value of α_{bl}, the images were enhanced and expanded, so the boundary of the bubble layer could be accurately obtained. Therefore uncertainty associated to α is considered to be 2 pixels (0.021 mm).

Conclusions

The presence of microbubbles within the critical zone of the buffer layer yields a drag reduction similar to the results obtained from drag reduction due to the addition of surfactants and polymers. The thickening of the viscous zone and upward shifts of the logarithmic region are observed. It was also shown that the microbubble layer formed at the channel top wall has no major role in drag reduction. The present data suggest that the most important aspect in achieving high drag reductions is the accumulation of microbubbles in a critical zone in the buffer layer, from $y^+ \approx 15$ to $y^+ \approx 30$. It indicates that there is a minimum critical microbubble void fraction necessary to achieve drag reductions of about 20% or higher. It is the first time, to our knowledge, that high percentage drag reductions can be achieved with low local void fractions.

The vorticity fields also show similarities to drag reduction characteristics by polymer and surfactant injection. The reduction of vorticity magnitude occurs close to the wall as the drag reductions increases. The modification of the normal and streamwise components of the mean velocity vector across the two-phase boundary layer has been presented and discussed. It is shown that for the high drag reduction cases the normal velocity component shifts away from the wall indicating a positive value of the normal velocity component. This phenomenon is not clear yet for the low drag reduction cases, where measurement uncertainty could be an important issue. The results obtained so far lead to the conclusion that drag reduction by microbubble injection is not a simple consequence of density effects, but is an active and dynamic interaction between the turbulence structure in the buffer zone and the microbubbles concentration in this region.

Acknowledgment

Acknowledgement is due to the reviewers of this paper, for their valuable comments and suggestions.

References

[1] Kodama, Y., Kakugawa, A., Takahashi, T., and Kawashima, H., 2000, "Experimental Study on Microbubbles and Their Applicability to Ship for Skin Friction Reduction," Int. J. Heat Fluid Flow, **21**, pp. 582–588.

[2] Gad-el-Hak, M., 2000, *Flow Control: Passive, Active and Reactive Flow Management*, Cambridge University Press, Cambridge, England.

[3] McCormick, M. E., and Bhattacharyya, R., 1973, "Drag Reduction on a Submersible Hull by Electrolysis," Nav. Eng. J., **85**, pp. 11–16.

[4] Sanders, W. C., Ivy, E. M., Ceccio, S. L., Dowling, D. R., and Perlin, M., 2003, "Microbubble Drag Reduction at High Reynolds Number," *4th ASME JSME Joint Fluids Engineering Conference*, Honolulu, HI, Paper No. FEDSM2003-45649.

[5] Madavan, N. K., Deutsch, S., and Merkle, C. L., 1984, "Reduction of Turbulent Skin Friction by Microbubbles," Phys. Fluids, **27**, pp. 356–363.

[6] Fontaine, A., Deutsch, S., Brungart, T. A., Petrie, H. L., and Fenstermacker, M., 1999, "Drag Reduction by Coupled Systems: Microbubble Injection with Homogeneous Polymer and Surfactant Solutions," Exp. Fluids, **26**, pp. 397–403.

[7] Takahashi, T., Kakugawa, A., Kodama, Y., and Makino, M., 2001, "Experimental Study on Drag Reduction by Microbubbles Using a 50m-Long Flat Plate Ship," *Second International Symposium on Turbulence and Shear Flow Phenomena*, 1, Stockholm, Sweden, pp. 175–180.

[8] Kawamura, T., Moriguchi, Y., Kato, H., Kakugawa, A., and Kodama, Y., 2003, "Effect of Bubble Size on the Microbubble Drag Reduction of a Turbulent Boundary Layer," *4th ASME JSME Joint Fluids Engineering Conference*, Honolulu, HI, Paper No. FEDSM2003-45645.

[9] Madavan, N. K., Deutsch, S., and Merkle, C. L., 1985, "Measurements of Local Skin Friction in a Reynolds Bubble-Modified Turbulent Boundary Layer." J. Fluid Mech., **156**, pp. 237–256.

[10] Legner, H. H., 1984, "A Simple Model for Gas Bubble Drag Reduction," Phys. Fluids, **27**, pp. 2788–2790.

[11] Kitagawa, A., Sugiyama, K., Ashihara, M., Hishida, K., and Kodama, Y., 2003, "Measurement of Turbulence Modification by Microbubbles Causing Frictional Drag Reduction," *4th ASME JSME Joint Fluids Engineering Conference*, Honolulu, HI, Paper No. FEDSM2003-45648.

[12] Madavan, N. K., Merkle, C. L., and Deutsch, S., 1985b, "Numerical Investigations into the Mechanisms of Microbubble Drag Reduction," ASME J. Fluids Eng., **107**, pp. 370–377.

[13] Xu, J., Maxey, M. R., and Karniadakis, G., 2002, "Numerical Simulation of Turbulent Drag Reduction Using Micro-Bubbles," J. Fluid Mech., **468**, pp. 271–281.

[14] Ferrante, A., and Elghobashi, S., 2004, "On the Physical Mechanisms of Drag Reduction in a Spatially Developing Turbulent Boundary Layer Laden with Microbubbles," J. Fluid Mech., **503**, pp. 345–355.

[15] Arakawa, K., Toda, K., and Yamamoto, M., 2003, "Modeling and Computational Study on Microbubble Two-Phase Turbulent Flow," *4th ASME JSME Joint Fluids Engineering Conference*, Honolulu, HI, Paper No. FEDSM2003-45760.

[16] Kunz, R. F., Deutsch, S., and Lindau, J. W., 2003, "Two Fluid Modeling of Microbubble Turbulent Drag Reduction," *4th ASME JSME Joint Fluids Engineering Conference*, Honolulu, HI, Paper No. FEDSM2003-45640.

[17] Yamamoto, Y., Gobara, R., and Uemura, T., 2001, "High-Efficiency Particle Detection Method Using 1D-correlation," *3rd Pacific Symposium on Flow Visualization and Image Processing*, Maui, HI, Paper No. F3130.

[18] Uemura, T., Yamamoto, F., and Ohmi, K., 1991, "Mixing Flow in a Cylindrical Vessel Agitated by a Bubbling Jet," *Application of Laser Techniques to Fluid Mechanics*, Springer-Verlag, Berlin, pp. 512–536.

[19] Stalisnas, M., Okamoto, K., and Kähler, C., 2003, "Main Results of the First International PIV Challenge," Meas. Sci. Technol., **14**, pp. R63–R89.
[20] Hassan, Y. A., Blanchat, T. K., Seeley, Jr.C. H., and Canaan, R. E., 1992, "Simultaneous Velocity Measurements of Both Components of a Two-Phase Flow Using Particle Image Velocimetry," Int. J. Multiphase Flow, **18**, pp. 371–395.
[21] Djenidi, L., Dubief, Y., and Antonia, R. A., 1997, Advantages of Using a Power Law in a Low R_θ Turbulent Boundary Layer," Exp. Fluids, **22**, pp. 348–350.
[22] Durst, F., Kikura, H., Lekakis, I., Jovanovic, J., and Ye, Q., 1996, "Wall Shear Stress Determination from Near-Wall Mean Velocity Data in Turbulent Pipe and Channel Flows," Exp. Fluids, **20**, pp. 417–428.
[23] Schlichting, H., and Gersten, K., 2000, *Boundary Layer Theory*, 8th ed., Springer, New York.
[24] Warholic, M. D., Massah, H., and Hanratty, T. J., 1999, "Influence of Drag-Reducing Polymers on Turbulence: Effects of Reynolds Number, Concentration and Mixing," Exp. Fluids, **27**, pp. 461–472.
[25] White, C. M., Somandepalli, V. S. R., and Mungal, M. G., 2004, "The Turbulence Structure of Drag-Reduced Boundary Layer Flow," Exp. Fluids, **36**, pp. 62–69.
[26] Dubief, Y., White, C. M., Terrapon, V. E., Shaqfeh, E. S. G., Lele, S. K., and Moin, P., 2003, "Numerical Simulation of High Drag Reduction Regime in Polymer Solutions," *4th ASME JSME Joint Fluids Engineering Conference*, Honolulu, HI, Paper No. FEDSM2003-45652.
[27] Udrea, D. D., Bryanston-Cross, P. J., Moroni, M., and Querzoli, G., 2000, "Particle Tracking Velocimetry Techniques," *Particle Image Velocimtery. Progress towards Industrial Application*, Kluwer Academic, Dordrecht, The Netherlands, pp. 279–304.